

## ANGULAR ENERGY DISTRIBUTION OF COLLAPSAR-JETS

AKIRA MIZUTA<sup>1</sup>, AND MIGUEL A. ALOY<sup>2</sup>,  
*accepted for publication in ApJ*

### ABSTRACT

Collapsars are fast-spinning, massive stars, whose core collapse liberates an energy, that can be channeled in the form of ultrarelativistic jets. These jets transport the energy from the collapsed core to large distances, where it is dissipated in the form of long-duration gamma-ray bursts. In this paper we study the dynamics of ultrarelativistic jets produced in collapsars. Also we extrapolate our results to infer the angular energy distribution of the produced outflows in the afterglow phase. Our main focus is to look for global energetical properties which can be imprinted by the different structure of different progenitor stars. Thus, we employ a number of pre-supernova, stellar models (with distinct masses and metallicities), and inject in all of them jets with fixed initial conditions. We assume that at the injection nozzle, the jet is mildly relativistic (Lorentz factor  $\sim 5$ ), has a finite half-opening angle ( $5^\circ$ ), and carries a power of  $10^{51}$  erg s<sup>-1</sup>. In all cases, well collimated jets propagate through the progenitor, blowing a high pressure and high temperature cocoon. These jets arrive intact to the stellar surface and break out of it. A large Lorentz factor region  $\Gamma \gtrsim 100$  develops well before the jet reaches the surface of the star, in the unshocked part of the beam, located between the injection nozzle and the first recollimation shock. These high values of  $\Gamma$  are possible because the finite opening angle of the jet allows for free expansion towards the radial direction. We find a strong correlation between the angular energy distribution of the jet, after its eruption from the progenitor surface, and the mass of the progenitors. The angular energy distribution of the jets from light progenitor models is steeper than that of the jets injected in more massive progenitor stars. This trend is also imprinted in the angular distribution of isotropic equivalent energy.

*Subject headings:* hydrodynamics - jet - GRBs - supernovae - shock - relativity

### 1. INTRODUCTION

Recent observations of gamma-ray bursts (GRBs) suggest that long duration GRBs and type Ib/c supernova (SN) explosions are tightly connected. For example, SN1998bw was observed in the positional error box of GRB980425 (Galama et al. 1998). In this case the GRB/SN association was based on the spatial and temporal coincidence of both events. The most remarkable example of long GRB/SN link came in 2003, when the spectra of both the GRB030329 afterglow and of the SN2003dh were measured, since the burst happened closeby and it was quite bright. The supernova spectrum, which includes many complex lines, gradually appeared from the decaying afterglow spectrum after a few tens of days from the burst. The spectrum of SN2003dh after about a month from the explosion is quite similar with that of SN1998bw at the same stage. Both SN1998bw and SN2003dh are type Ic supernovae (Iwamoto et al. 1998; Stanek et al. 2003) whose progenitor had lost the hydrogen and the helium envelopes during the pre-supernova stage. They are also categorized within a special class of supernova explosions, so-called hypernovae, whose explosion energy is about ten times higher, i.e.,  $\sim 10^{52}$  erg, than that of ordinary supernova. Indeed, our common view is that most long-lasting GRBs are produced by core-collapse supernovae akin to SN1998bw.

GRBs are not exclusively linked to hypernovae. For instance, the long lasting burst ( $t_d \sim 2 \times 10^3$  s) GRB060218 (or XRF060218) was associated with the type Ic SN2006aj, which is not a hypernova. The explosion energy falls within the regular range for type Ic events (Campana et al. 2006). Mazzali et al. (2006) argued that the progenitor star may not form a black hole but a neutron star, since the estimated mass of the progenitor during the main sequence is  $\sim 20M_\odot$ . On the other hand, there are recent examples of cases of long-lasting GRBs (GRB060505 and GRB060614) where no supernova signature was observed at all even if, considering the distance, the observational trace of a supernova should have been detected (Fynbo et al. 2006; Della Valle et al. 2006; Gal-Yam et al. 2006).

Though a variety of long duration GRBs which have a strong connection with SNs are observed, we still lack of a complete picture of the processes by which a sizable fraction of the energy involved in a type Ib/c SN explosion is tapped in a relatively narrow channel, and produces a GRB at a large distance from the original site of generation. Rees & Meszaros (1992) proposed that the death of massive stars can be an origin of GRBs. Woosley (1993) introduced the collapsar model to account for the progenitor system of long GRBs. According to this model, a non-spherical outflow could be formed from the deep inside of the progenitor where a black hole or a proto-neutron star is born as a result of the collapse of the iron core (MacFadyen & Woosley 1999). If the specific angular momentum of the iron core is sufficiently large, an accretion torus may develop around the central compact object. The system formed by a central object and

Electronic address: AM, e-mail: mizuta@cfs.chiba-u.ac.jp  
<sup>1</sup> Center for Frontier Science, Chiba University Yayoi-cho 1-33, Inage-ku, Chiba, 263-8522 Japan  
<sup>2</sup> Departamento de Astronomía y Astrofísica, Universidad de Valencia, 46100-Burjassot (Valencia), Spain

an accretion disk has the potential to launch a bipolar outflow.

The mechanisms proposed to extract energy out of such central engines are basically two (e.g., Aloy & Obergaulinger 2007): thermal or hydromagnetic. Thermal mechanisms rely on depositing a considerable amount of thermal energy in the vicinity of the rotation axis of the system, just above the poles of the central compact object, where a low density funnel has develop in the course of the evolution. The accretion energy of the hot torus is converted into a copious flux of neutrinos  $\nu$  and anti-neutrinos  $\bar{\nu}$ . From the  $\nu\bar{\nu}$ -annihilation a hot  $e^+e^-$ -plasma results. In its turn,  $e^+e^-$ -pairs annihilate yielding a *fireball* of high energy photons. The conversion of the thermal energy of the fireball into kinetic energy partly determines the subsequent evolution of the plasma. It accelerates to ultrarelativistic speeds (reaching Lorentz factors of  $\sim 50$  Aloy et al. 2000) while, at the same time, interacts with the progenitor system. Alternatively, MHD process may tap a fraction of the rotational energy of the BH or of the accretion disk to form an outflow (Proga et al. 2003; Mizuno et al. 2004; McKinney 2006; Nagataki et al. 2007; Komissarov & Barkov 2007; Takiwaki et al. 2009).

A number of works have dealt with the hydrodynamic properties of the outflows generated in collapsar progenitors as they propagate through the progenitor system (and in some cases beyond the surface of the progenitor star). The problem is addressed by means of numerical relativistic hydrodynamic simulations with different degrees of complexity (Zhang et al. 2003, 2004; Mizuta et al. 2006; Morsony et al. 2007; Tominaga et al. 2007), which assume that a quasi-steady momentum flux has been produced at a certain distance from the region where the energy is released (independent of which is the actual energy extraction mechanism -MHD or thermal-). Therefore, such numerical works assume the existence of a nozzle through which the injection of a supersonic jet is produced, and put their focus on the modification of the morphology and of the dynamics of collimated outflows as they travel through the progenitor star. Depending on the exact inflow conditions, a variety of different outflows result. For instance, Mizuta et al. (2006) finds a whole spectrum of outflows ranging from collimated, relativistic jets to poorly collimated expanding winds. Thus, Mizuta et al. argue that such a variety of resulting outflows supports the idea that the same collapsar scenario can yield a number of different phenomena (in agreement with the previous ideas of unification of high energy transients, e.g., Ramirez-Ruiz et al. 2002b), such as, GRBs, X-ray rich GRBs, X-ray Flashes, and normal supernovae.

In the prompt GRB phase we observe the emission of high energy photons from an ultrarelativistic outflow, which is generated at a distance  $10^{13-15}$  cm, very far from the central engine. Due to the large optical thickness of the outflow at scales comparable to that of the progenitor, we have not observed any electromagnetic emission directly from the progenitor so far, except, perhaps, some precursor activity (Woosley 2000; Ramirez-Ruiz et al. 2002a). Since the direct detection of progenitors of GRBs is nowadays impossible (if they happen at cosmological distances), the observation of the association between

GRBs and SNe probably provides the best clue to understand the progenitors of the GRBs. Though more than 100 GRBs per year are identified, most of them occur far away. Thus, it is technically impossible to identify their accompanying supernovae. Another clue regarding the nature of the GRB progenitors comes from the environment and the host galaxies in which the burst takes place. Both clues indicate that long-duration GRBs are associated with the death of the most massive stars (Fruchter et al. 2006). The typical hosts of long GRBs are star-forming, low metallicity galaxies (with an star formation rate  $\sim 10^3 M_{\odot}y^{-1}$ ; Berger, Kulkarni, & Frail 2001; Frail et al. 2002) but bluer than typical starburst galaxies, with little dust (Le Floch 2004), and lower masses than current ellipticals, i.e., they correspond to the typical environments of formation of massive stars. Fruchter et al. (2006) also conclude, that the host galaxies of the GRBs are significantly fainter and more irregular than the hosts of core-collapse supernovae.

A very interesting question is whether it is possible to get any information on the nature of a GRB progenitor from the observation of the afterglow emission. One possibility is to look at the angular distribution of integrated energy per unit of solid angle, as observed in the afterglow phase of the burst. Lazzati & Begelman (2005) estimated theoretically such an angular distribution assuming, that the kinetic energy of the jet is converted to thermal energy in the cocoon, till the head of the jet reaches the progenitor surface. The cocoon originates from jet material which crosses through the terminal strong shock of the collimated outflow and moves away from the center of the progenitor surrounding the beam of the jet. A fat cocoon develops for light jets, i.e., jets whose rest-mass density is much lower than that of the ambient gas into which the jet propagates. When the jet breaks out the progenitor surface, the thermal energy is released to a low-density inter stellar medium (ISM). Lazzati & Begelman (2005) concluded, that the energy distribution per solid angle ( $dE/d\Omega$ ) of the jet displays a  $\theta^{-2}$  dependence with the viewing angle after its eruption through the progenitor surface. Recently, Morsony et al. (2007) have used hydrodynamic simulations to test the theoretical prediction of Lazzati & Begelman, and found that their numerical models do not follow the inferred theoretical angular energy distribution.

In this paper we also try to verify the analytic relation for the angular dependence of the energy with the polar angle that was proposed by Lazzati & Begelman (2005). We explore a parameter space different from that of Morsony et al. (2007) in order to compute the dependence of the angular energy distribution on the structure of the progenitor. The progenitor models are built upon the pre-supernova models of Woosley & Heger (2006). Along the way, we also characterize the hydrodynamic properties of relativistic jets propagating through different progenitor stars.

The paper is organized as follows. We describe our physical model, the choice of stellar progenitors, and relevant numerical details in Sect. 2. In the appendix, we provide a study of a selected sample of models in order to justify our choice of numerical resolution and the effects it has on our conclusions. The dynamics of the injected bipolar outflows, and the extrapolated angular

energy distribution in the afterglow phase is considered in Sec. 3. Finally, we discuss our results and write down the conclusions of this work in Sect. 4.

## 2. MODEL

We will investigate the dependence of the properties of relativistic jets, injected in a pre-supernova stellar model at a certain distance from the center, using relativistic hydrodynamic simulations. In Sect. 2.1 we show the different stellar progenitors used in this study. We provide the technical details of the numerical simulations in Sect. 2.2. Finally, in Sect. 2.3 we specify the physical conditions used to inject relativistic jets in the pre-supernova progenitors described above.

### 2.1. Progenitors

In the last years, some detailed calculations of stellar evolution of massive stars have been done including the effects of initial angular momentum, dynamo, metallicity, and mass loss rate (Yoon & Langer 2005; Yoon et al. 2006; Woosley & Heger 2006). According to these studies, the metallicity of the progenitor strongly affects the evolution of the angular momentum distribution at the pre-supernova stage, in such a way, that low metallicity is preferred to obtain a large angular momentum in the core of the progenitor.

For the purposes of this work, we employ some of the pre-supernova models computed by Woosley & Heger (2006). We stick to the same naming convention than the former authors, and consider several sets of models (Tab. 1). The first group corresponds to the HE16-series of 16 models of Woosley & Heger, which include progenitor stars for which  $16M_{\odot}$  bare helium cores are evolved, that have solar metallicity, and different amounts of initial angular momentum, dynamo effects, mass-loss rates, etc. The last three models of Tab. 1, 16OC, 16TB, and 16TC form the second group of progenitors. They correspond to stars with the same initial mass as those of the first group but with a smaller metallicity ( $Z_{16OC} = 0.1Z_{\odot}$ ,  $Z_{16TB} = Z_{16TC} = 0.01Z_{\odot}$ ). The second set of low-metallicity models has been chosen among the many other possibilities available because their radius, at the pre-supernova stage, are the smallest among all other low-metallicity progenitors (in all cases, their stellar radii are  $R_* < 10^{11}$  cm).

Figure 1 shows the radial mass profiles of the models HE16C, HE16L, and HE16N. HE16C is representative of progenitors whose pre-supernova mass is small  $M_{\text{HE16C}} \simeq 5M_{\odot}$  (due to the vigorous mass loss rate in the late phases of its evolution; Tab. 1). Other members of this group of low pre-supernova mass are HE16B, HE16J, and HE16K. We will refer to this group as type-L. The model HE16N belongs to the group of more massive progenitors ( $M_{\text{HE16C}} \simeq 15M_{\odot}$ ), to which we will refer as type-H models. Finally, the model HE16L (also HE16D) falls in the middle of these two groups (members of this group will be called type-M models). Its total mass is about  $9.5M_{\odot}$ . Figure 2 shows radial mass density profiles of the low metallicity models 16TB, 16TC, and 16OC. Though the mass of the models is similar ( $\sim 15.3M_{\odot}$ ), the density profiles are slightly different. In total, 19 models are considered in this study (Tab. 1). We neglect for the progenitors any deviation from spherical symmetry arising from the rotation of the models.

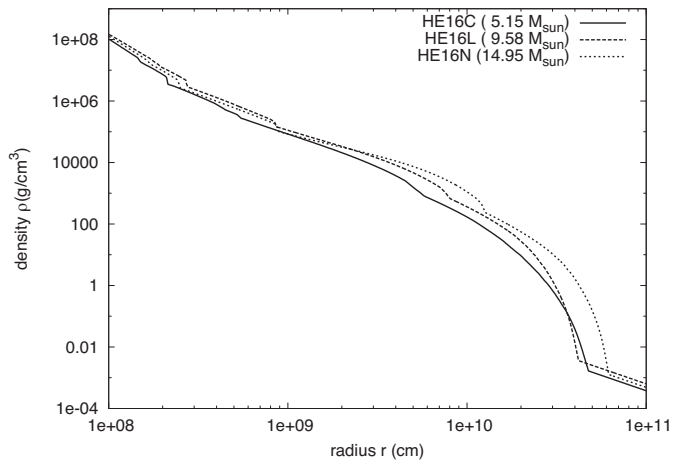


FIG. 1.— Radial mass profiles of models HE16C, HE16L and HE16N.

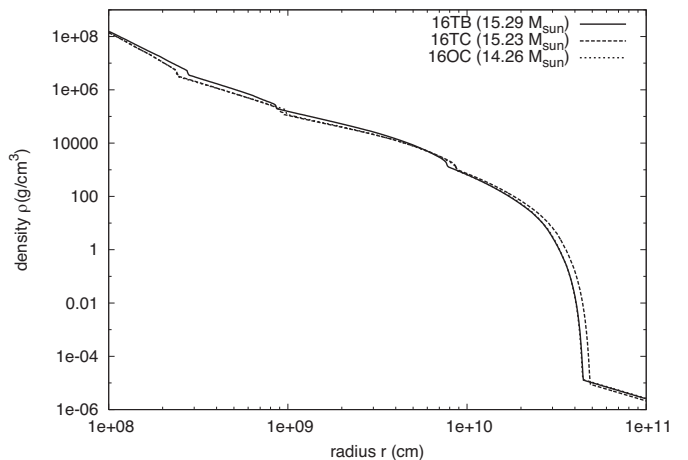


FIG. 2.— Radial mass profiles of models 16TB, 16TC and 16OC.

Therefore, for the study we present here, each progenitor differs from the other mainly in its total mass, radius, and mass density profile at the pre-supernova stage.

Though a nonspherical structure is expected around the black hole due to the rapid rotation of the progenitor, it is reasonable to assume spherical symmetry for the envelopes of the progenitor for radial distances  $r \gtrsim 10^8$  cm, which is where we put the innermost radial boundary in the numerical simulations of this study. Thus, we only take from the models of Woosley & Heger (2006) the radial density and the radial velocity profiles which result by the end of the pre-supernova evolution. We assume that the pressure of the progenitor is very low, or, equivalently, that the initial specific internal energy ( $\epsilon$ ) is set to be very low ( $\epsilon/c^2 = 10^{-6}$ , where  $c$  is the speed of light).

Both the gravitational force produced by the central compact object, and the progenitor self gravity are ignored, since the timescale for the outflows to cross the progenitor and to break out from the surface of the progenitor,  $\sim 3s$ , is much shorter than free fall timescale for the stellar envelopes.

We extend the radial mass density profile to the outside

of the progenitor up to the outer computational boundary located at  $r_{\max} = 10^{11}$  cm. For the models which barely lose mass during the latest stages of their evolution, the rest-mass density is assumed to be uniform ( $\rho_{\text{ISM}} = 10^{-6}$  g cm $^{-3}$ ) and much smaller than that at the progenitor surface. If the progenitor star has a non-null mass loss rate (i.e., if the parameter  $a > 0.01$ , according to the nomenclature of Woosley & Heger 2006), we take a  $r^{-2}$  dependence in radial mass-density profiles from the surface of the progenitor (see Fig. 1).

## 2.2. Computational Domain and Basic Equations

We map the spherically symmetric progenitor models of Sect. 2.2 into a two-dimensional grid in spherical coordinates ( $r \times \theta$ ). We assume that our models are axial and equatorially symmetric and, therefore, specify reflection boundary conditions at the polar axis ( $\theta = 0^\circ$ ) and at the equator ( $\theta = 90^\circ$ ). The radial grid consists of  $N_r = 1000$  points, uniformly spaced in  $\log r$ , which extends from  $r_{\min} = 10^8$  cm to  $r_{\max} = 10^{11}$  cm. The smallest radial grid spacing, besides  $r_{\min}$ , is  $\Delta r_{\min} = 10^6$  cm, while the largest one, besides  $r_{\max}$ , is  $\Delta r_{\max} = 6.5 \times 10^8$  cm. The resolution we have chosen here represents a trade-off between accuracy and feasibility of the numerical simulations, as we discuss in the Appendix. Free outflow (i.e., zero gradient) boundary conditions are set at  $r = r_{\min}$  and  $r_{\max}$ . The polar grid has  $N_\theta = 180$  grid points uniformly spaced in the range  $0^\circ < \theta < 90^\circ$ , ( $\Delta\theta = 0.5^\circ$ ). We use the same 2D special relativistic hydrodynamic code of Mizuta et al. (2004, 2006) to perform our simulations. The code provides 3rd order accuracy in both space and time, by applying a PPM intra-cell interpolation and a TVD-Runge Kutta time integration. For the sake of simplicity, we employ an ideal gas equation of state ( $p = (\gamma - 1)\rho\epsilon$ ) with uniform adiabatic index  $\gamma = 4/3$ , where  $p$ ,  $\rho$  and  $\epsilon$  are the pressure and the rest-mass density, respectively.

## 2.3. Jet Injection Conditions

We assume that a jet has been generated by the central engine, and that at a certain distance, quasi-steady injection conditions are settled through a well defined circular nozzle. Thus, we inject plasma, in the radial direction, through the innermost radial boundary at  $r = r_{\min}$  in a cone of half-opening angle  $\theta_j = 5^\circ$ . The jet injection proceeds for a period  $t_{\text{inj}} = 4$  s. We parametrize the outflowing plasma by assuming that it is hot (we set  $\epsilon_j/c^2 = 30$ ) and moderately relativistic (the Lorentz factor being  $\Gamma_{j,0} = 5$ ). We adopt the convention that the parameters of the outflow at the injection point are named with a subscript 'j'. Because of the conversion of thermal-to-kinetic energy, the injected flows have the potential to accelerate to bulk Lorentz factors larger than 100 (Mizuta et al. 2006). During the first 3 s, the power of the injected outflow is  $L_{j,0} \equiv \rho_j \Gamma_{j,0} v_{rj} (h_j \Gamma_{j,0} - 1) c^2 \Delta S = 10^{51}$  erg s $^{-1}$ , where  $\Delta S$  is the area of the injection surface,  $h(\equiv 1 + \epsilon/c^2 + p/\rho c^2)$  is the specific enthalpy, and  $v_r$  is the radial component of the 3-velocity. The density and pressure of the injected outflow are obtained by setting  $\Gamma_{j,0}$ ,  $\epsilon_j$ ,  $L_{j,0}$ ,  $\theta_j$ , and  $r_{\min}$ . We fix  $L_{j,0} = 10^{51}$  erg s $^{-1}$ , which is higher than that adopted in previous studies (Zhang et al. 2003, 2004; Morsony et al. 2007). The total injected energy is several times  $10^{51}$  erg. Since the

main purpose of this study is to see the jet propagation and expansion of the cocoon into the interstellar medium after the shock breakout, we adopt this power to obtain a rapid propagation of the jet in the progenitor. This fast propagation is necessary to be consistent with the fact that we neglect the self-gravity of the star. If the jet crosses the progenitor much faster than the typical hydrodynamic timescale in the system, the progenitor remains roughly unchanged during the complete jet propagation through it and, therefore, we do not need to care about the progenitor evolution during such short timescales.

After the initial phase of constant kinetic power injection, both the kinetic power and the injection Lorentz factor are linearly decreased according to the laws  $L_j(t) = \max\{L_{j,0}(4 - t), 10^{49}$  erg s $^{-1}\}$ , and  $\Gamma_j(t) = \max\{\Gamma_{j,0} + 12 - 4t, 1.01\}$ , respectively, for  $3 \text{ s} < t < 4 \text{ s}$ . In this period of decaying injection power, the specific energy is kept fixed to the same value as it had at  $t = 0$ , and the density and the pressure are obtained from the other parameters (as in the constant injection power phase). After  $t = 4$  s, the flow injection ceases.

With the parametrization considered above, the rest-mass density ( $\rho_{j,0}$ ) during the constant power phase is  $154$  g cm $^{-3}$ . Since the rest-mass density of the progenitor around the inner computational boundary is  $\sim 10^8$  g cm $^{-3}$ , the injected outflow is initially much lighter than medium in which it is injected. Thus it is expected that the jet propagation velocity across the progenitor is smaller than the speed of light, and one naturally expects to generate relatively thick cocoons surrounding the beam of the jet.

## 3. RESULTS

### 3.1. Dynamics

The dynamical evolution of our jet models can be split in two phases. The first one happens during the period in which the jet drills its way through the progenitor star. The second one shows up latter, when the jet breaks out of the stellar surface. The dynamics of our models during this two phases is roughly similar to that outlined by some previous works (e.g., Aloy et al. 2000; Zhang et al. 2003, 2004; Mizuta et al. 2006; Morsony et al. 2007) and, therefore, we limit ourselves here to provide a shallow description of the most salient features.

Figure 3 shows a snapshot of the evolution of the density of the model HE16N at  $t = 1.0$  s, when the head of the jet is still in the progenitor. The left panel of the Fig. 4 shows the Lorentz factor contour at the same time shown in Fig. 3. The jet is well collimated both inside of the progenitor and as it travels through the ISM. The bow shock develops close to the head of the jet and rises the pressure and the temperature of the envelope region it sweeps up (in agreement with the findings of Mizuta et al. 2004). It takes about 3.2 s for the jet to cross the progenitor, hence, the average propagation velocity is  $\sim 0.63c$ . The right panel of Fig. 4 shows the Lorentz factor of the model HE16C at  $t = 0.7$  s, showing that the head of the jet in model HE16C propagates faster than model HE16N due to the lower density in model HE16C.

Although the outflow has a finite initial opening angle, the the beam of the jet is almost parallel to the polar

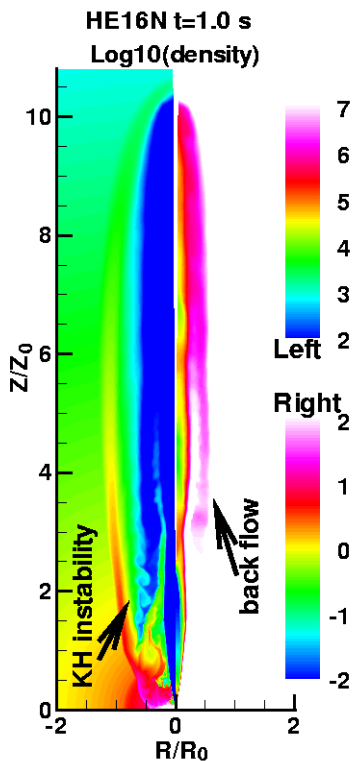


FIG. 3.— Snapshot (at  $t = 1.0$  s) of the rest-mass density of model HE16N. The left and right panels are shown with different color scales in order to outline the most salient features of the cocoon and the cavity drilled by the jet (left), and to show more clearly the structure of the beam (right). Both, the vertical and the horizontal axis are scaled by  $R_0 = Z_0 = 10^9$  cm. A strong bow shock surrounds the jet, the cocoon, and the shocked progenitor gas. A vigorous back flow from the head of the jet can be seen. Some vortices caused by Kelvin-Helmholtz instabilities are also indicated in the figure.

axis. The kinetic energy of the beam is dissipated when it crosses the reverse shock (i.e., the Mach disc) at the head of the jet. After the beam plasma is decelerated at the Mach disc and its pressure is risen to a much higher value than in the beam, it expands and flows back in a thick cocoon. The high pressure of the cocoon is the responsible for the beam collimation during the initial phase of propagation inside of the progenitor star. Also during this early stage of the evolution, a strong backflow can be seen flanking the beam of the jet. Some vortices develop between the jet and the backflow caused by the growth of Kelvin-Helmholtz modes. An schematic view of this process can be seen in Fig. 5a of Mizuta et al. (2006).

The propagation of the jet inside the progenitor also drives a cavity limited by a shroud whose density and pressure is larger than in the cocoon. The shroud is swept up by a reverse shock that results from the interaction between the cavity and the progenitor envelope. However, this reverse shock is not strong enough to rise the temperature above the threshold in which nuclear reactions can take place.

After the jet breaks out the progenitor surface, it proceeds to the ISM, which is assumed to be rarefied for model HE16N. In this phase, cocoon is almost freely released into the ISM, because of the negligible pressure of

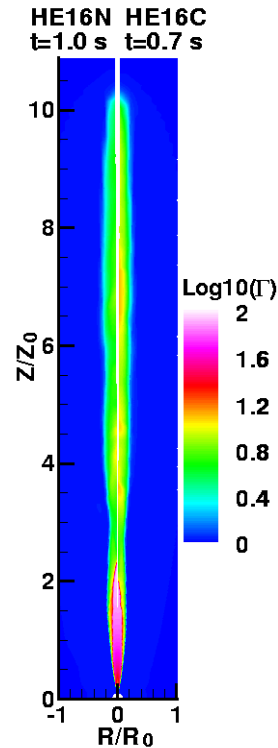


FIG. 4.— Lorentz factor contours of two models (left: model HE16N at  $t = 1.0$  s, and right HE16C at  $t = 0.7$  s). Both, the vertical and the horizontal axis are scaled by  $R_0 = Z_0 = 10^9$  cm. The largest Lorentz factors are reached close to the polar axis where the first reconfinement shock appears. Some weak reconfinement shocks can also be seen further downstream.

the external medium (Fig. 5). In spite of the fact that the inertial confinement provided by the stellar progenitor is lost in the ISM, by the time the jet reaches the surface of the star, the beam has accelerated to  $\Gamma \gtrsim 40$  (see Sect. 3.1.1) and, thus, it has entered into a ballistic regime, where lateral expansion is strongly suppressed. Thereby, the jet remains well collimated as it propagates through the ISM, and the half-opening angle of the beam reaches only a few degrees. These collimation properties have been confirmed by means of numerical models with better resolution in the  $\theta$ -direction (see Appendix).

### 3.1.1. Acceleration to High Lorentz Factor

In this section we focus on the dynamics of the acceleration of the flow to large Lorentz factors  $\Gamma \gtrsim 100$ , as requested by the standard fireball model (e.g., Piran 1999). Within such a theoretical model, an initial release of thermal energy is later converted into kinetic energy of the flow, as it expands into a dilute and cold environment. On the basis of this model, a number of numerical results have assessed that a jet, injected through a pre-established nozzle, is able to drill its way through a collapsar can reach an ultrarelativistic regime under likely inflow conditions (Zhang et al. 2003, 2004; Mizuta et al. 2006; Morsony et al. 2007, and this paper). We focus here on the details of the dynamical phase in which a kinematically mildly relativistic jet ( $\Gamma_j \sim 5$ ) speeds up to the ultrarelativistic regime  $\Gamma \gtrsim 100$  converting its initial (thermal) energy  $\epsilon_j/c^2 \gg 1$  into kinetic energy.

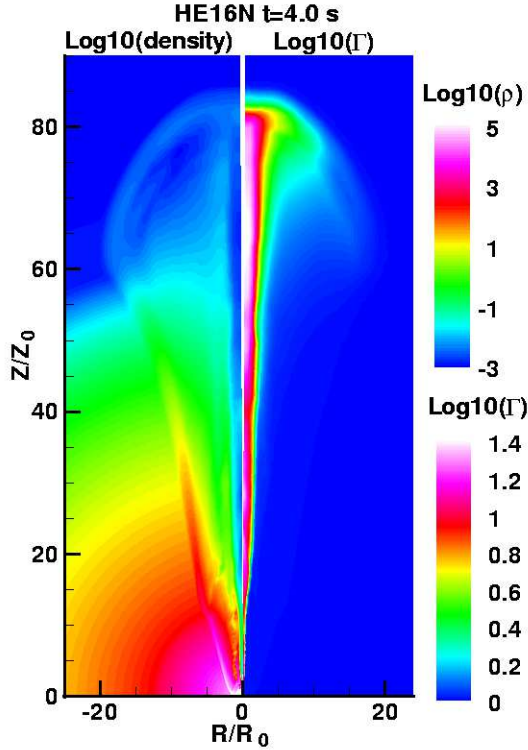


FIG. 5.— Density and Lorentz factor contours of the model HE16N at  $t = 4$  s. Both, the vertical and the horizontal axis are scaled by  $R_0 = Z_0 = 10^9$  cm. By this time, the head of the jet has already broken out of the progenitor surface, and the bow shock begins to expand into the ISM.

To drive the discussion, we take as a prototype case that of model HE16N. The acceleration process of other models is very similar. Figures 6a-6c show one dimensional profiles of density, pressure, and Lorentz factor along the polar axis, at different times. These profiles are qualitatively similar to the ones shown in previous papers (e.g., Aloy et al. 2002; Morsony et al. 2007). During the injection the Lorentz factor increases linearly (Fig. 6c), whereas both the density and pressure decrease as  $r^{-3}$  and  $r^{-4}$  (Fig. 6a, b), respectively. This is not unexpected, since the fluid expands radially (almost freely) in that region, where there are no shocks. Note that this result differs a bit from models where the generation of the outflow is considered (Aloy et al. 2000, 2002). If jet injection conditions are set through a nozzle at a certain distance to the center, the variability imprinted by the highly dynamical generation of the jet is erased. Clearly, this minimizes the number of internal shocks in the outflowing jet. Aloy et al. (2000) show in their Fig. 2 that the outflow can accelerate to Lorentz factors which are smaller than those attained in this work and in others where jet injection conditions are assumed. This is because of the modulation in the growth of the Lorentz factor imposed by the development of Kelvin-Helmholtz modes in the course of the very early outflow evolution (Aloy et al. 2002). Nevertheless, models which consistently include the outflow generation (by thermal energy deposition), can still accelerate to ultrarelativistic Lorentz factors at large distance from the source. In such models the flow is kept hotter than in the present ones

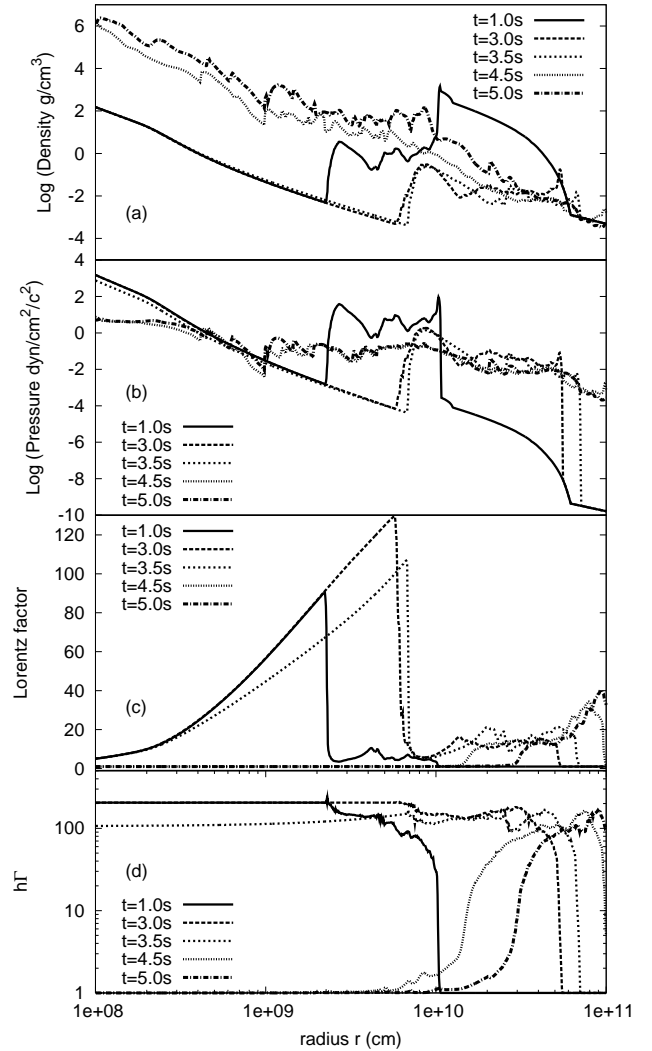


FIG. 6.— Profiles of the rest-mass density (a), of the pressure (b), of the bulk Lorentz factor (c), and of  $h\Gamma$  (d) along the polar axis at times  $t = 1.0, 3.0, 3.5, 4.5$  and  $5.0$  s (see legends), corresponding to model HE16N.

because of the occurrence of internal shocks already inside of the progenitor. However, since the outflow is optically thick, the thermal energy is not radiated away, but converted (later) into kinetic energy (Aloy et al. 2000; Aloy & Martí 2002; Ghisellini et al. 2007).

One can notice that the maximum Lorentz factor is reached behind the first recollimation shock in the jet (Figs. 4 and 6c) coinciding with the location of the minimum density in the beam of the jet (Figs. 3 and 6a). Inside of the progenitor star the jet reaches a maximum Lorentz factor  $\Gamma \gtrsim 100$  (see dashed line in Fig. 6c corresponding to  $t = 3$  s). We note that the quick acceleration to large Lorentz factor happening in the present models is a direct result of the fact that the flow is injected into a finite opening angle. Differently, Mizuta et al. (2006), who injected the jet parallel to the polar axis of the progenitor, did not find such a fast acceleration. In the later case, the occurrence of recollimation shocks much closer to the injection nozzle prevents the development

a freely expanding, unshocked jet extending so far away as in the models of this work. Indeed, such internal, recollimation shocks are the responsible of the confinement of the jet (Komissarov & Falle 1997, 1998; Mizuta et al. 2004, 2006; Mimica et al. 2008). Nonetheless, the head propagation speed is very similar in Mizuta et al. (2006) as it is found here and, hence, also the crossing time of the progenitor by the jet. In Mizuta et al. (2006) an acceleration of the jet to  $\Gamma \gtrsim 100$  at larger distances from the source happens (by thermal-to-kinetic energy conversion), but it still takes place inside of the progenitor star. This resembles more the acceleration process of outflows generated self-consistently from the inner engine as pointed out above.

The absolute maximum Lorentz factor ( $\Gamma_{\max} \sim 130$ ) is attained by the time we begin to reduce the luminosity of the inflow (at  $t = 3$  s, see § 2.2). By this time, the head of the jet has already broken up the surface of the progenitor. This numerical value is smaller than the maximum one which could be potentially reached, provided the conditions of the injected outflow, according to which  $\Gamma_{\max} \sim \Gamma_{j,0} h_j \simeq 205$ , which is an indication of the maximum potentially reachable Lorentz factor, along a flow line, if all thermal energy were converted to kinetic energy. After the energy deposition is switched off ( $t = 3$  s), the region previously occupied by the unshocked beam of the jet (up to the first recollimation shock of the beam; Fig. 6c) begins to shrink and to incorporate mass from its lateral boundaries (c.f., rest-mass density profiles between times 3.5 s and 5.0 s in Fig. 6a up to  $r \sim 8 \times 10^9$  cm). This fact reduces progressively both the beam Lorentz factor (Fig. 6c) and the ability of the beam fluid to reach large asymptotic values of  $\Gamma$  (Fig. 6d). Thereby, if the jet is injected with a finite half-opening angle, the ultrarelativistic part of the outflow (i.e., that where  $\Gamma \gtrsim 100$ ) may persist only if the activity of the engine does not cease.

### 3.2. Angular Energy Distribution

The evolution of our models has been followed until the head of the jet reaches the outermost radial computational boundary at  $r_{\max} = 10^{11}$  cm. At such distances, the outflow is still optically thick and, therefore, radiation cannot escape freely. The jet and the surrounding cocoon, past a transient phase, that happens after the jet breaks out of the stellar surface, enter into a quasi self-similar phase, where the properties of the outflow roughly scale with the distance of propagation and become almost time independent. This fact allows us to extrapolate the properties of the jet from distances  $r \simeq 10^{11}$  cm to the typical distances where the afterglow will take place (namely,  $r \simeq 10^{15}$  cm). Thus, we can roughly estimate the angular energy distribution per unit solid angle ( $dE/d\Omega$ ) that can be potentially emitted at the afterglow phase.

In order to derive  $dE/d\Omega$  we have to make several assumptions. First, we assume that a fix fraction (the same everywhere) of the total energy (internal plus kinetic) will be converted into electromagnetic radiation. Basically, this assumption is equivalent to state that the angular profile of the observed non-thermal radiation is simply a scaled version of the total energy angular profile. Certainly, this is a rough approximation, since the non-thermal radiation from  $\gamma$ -rays to radio fre-

quencies will be produced by synchrotron (and, perhaps, inverse Compton) processes of particles accelerated at shocks (or, maybe, along the jet boundary layer; e.g., Aloy & Rezzolla 2006). Obviously, there are shocks of very different properties in the ultrarelativistic beam and in the cocoon and, thus, we may expect somewhat different conversion efficiencies of the outflow energy into radiation in the beam and in the cocoon. Finally, we assume that the angular energy distribution is *frozen-in* by the time when the head of the jet reaches the outer computational boundary. As commented above, our models evolve almost self-similarly a bit after they break out of the stellar surface, and therefore, we expect only a minor time evolution of the angular profiles of  $dE/d\Omega$ .

We point out that the procedure we use to estimate  $dE/d\Omega$  differs from that of Morsony et al. (2007), who derived their  $dE/d\Omega$  profiles from the time integration of the energy flux trough a certain radius. Under the hypothesis of self-similar evolution, this is equivalent to integrate, along the radial direction, the energy density of our models (by the time they reach  $r_{\max}$ ) as follows,

$$\frac{dE}{d\Omega}(\theta) \equiv \sum_{k=-N_\theta}^{N_\theta} \sum_{i=i_*}^{N_r} \left( \frac{1 - \beta_{ik}^r}{1 - \beta_{ik}^r \cos(\theta - \theta_k)} \right)^3 \times (\rho_{ik} h_{ik} \Gamma_{ik}^2 - p_{ik} - \rho_{ik} \Gamma_{ik}) r_i^2 \Delta r_i, \quad (1)$$

where the subscripts  $i$  and  $k$  are associated to the spherical grid coordinates  $r_i$ , and  $\theta_k$ , respectively, and  $\beta^r$  and  $\theta$  are the radial velocity in units of  $c$  and the observer's viewing angle (measured from the jet axis), respectively. The expression (1) includes the radiation contributions coming from regions outside of the line of sight (see Janka et al. 2006). The summation in the radial direction runs from the surface of the progenitor, located at  $r = r_*$  or, equivalently,  $i = i_*$ , to the outermost boundary. The summation in the azimuthal angle runs from  $\theta = -90^\circ$  to  $\theta = 90^\circ$  (note that due to the assumed axial symmetry, we can copy the computed data of the quadrant  $0^\circ < \theta < 90^\circ$  to the quadrant  $-90^\circ < \theta < 0^\circ$ ). In order to avoid accounting for subrelativistic regions, which will not contribute to the afterglow energetics, we exclude the contributions of numerical cells where  $v_r < 0.7c$  and  $h\Gamma < 4$  in the expression (1).<sup>3</sup>

The absolute value of the observed  $dE/d\Omega(\theta)$  along every radial direction forming an angle  $\theta$  with the polar axis depends, among other things, on two parameters whose exact value is not well constrained, neither by observations nor by the present day theory. These are (i) the efficiency of energy conversion to radiation, and (ii) the total energy injected. Therefore, we will show only the angular profiles of  $dE/d\Omega(\theta)$  normalized to the maximum value  $dE/d\Omega(\theta)|_{\max}$  found for each model. Figure 7 shows the normalized angular energy distributions corresponding to models HE16C, HE16L and HE16N, which are prototypes of the types L, M and H, respectively. In the same figure we overplot fits to the normalized  $dE/d\Omega(\theta)$  profiles. The fitting function is a smoothly

<sup>3</sup> Note that numerical cells where  $h\Gamma < 4$  have the potential to accelerate, at most, to  $\Gamma \sim 4$ . In actuality, the asymptotic Lorentz factor of such parcels of fluid, will be much smaller, since they will decelerate as they incorporate mass from the external medium.

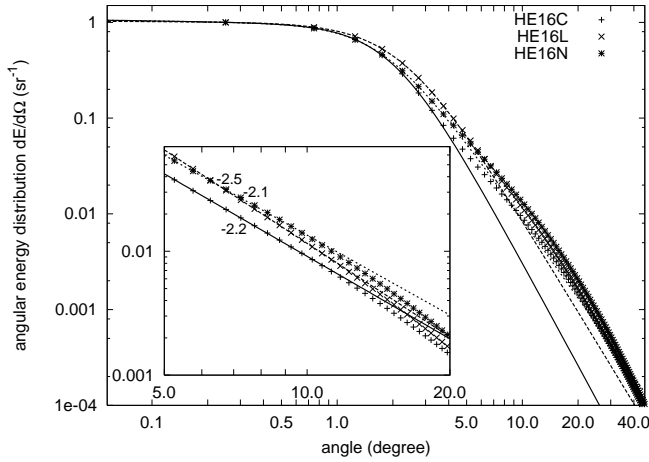


FIG. 7.— Angular energy distribution of models, HE16C, HE16L, and HE16N, when the head of the jet reaches the outer computational boundary. With lines we also show the fitting functions to SBPs (Eq. 2) for each model. The solid, dashed, and dotted lines are the fitting functions of Eq. 2 corresponding to models HE16C, HE16L, and HE16N, respectively. The inset displays a zoom of the angular range  $5^\circ < \theta < 20^\circ$ , where simple power law fitting functions are overplotted, along with the corresponding values of the power law indices. This angular region is dominated by the contribution of the expanding cocoon.

broken power law (SBP) of the form,

$$F(\theta) = 2^{-1/n} A \left[ \left( \frac{\theta}{\theta_0} \right)^{\alpha_l n} + \left( \frac{\theta}{\theta_0} \right)^{\alpha_h n} \right]^{1/n}, \quad (2)$$

where  $A$  is the value of the function  $F$  at  $\theta = \theta_0$ ,  $\theta_0$  is the angular location of the break point between the prebreak and postbreak power-laws, whose slopes are  $\alpha_l$  and  $\alpha_h$ , respectively, and  $n$  is a numerical factor that controls the sharpness of the break. Note that the maximum value of  $F$  occurs at

$$\theta_{\max} = \theta_0 \left( -\frac{\alpha_h}{\alpha_l} \right)^{1/[(\alpha_l - \alpha_h)n]}, \quad (3)$$

when  $\alpha_l \alpha_h < 0$ . Otherwise, if  $\alpha_l < 0$  and  $\alpha_h < 0$ , the function diverges as  $\theta \rightarrow 0$ .

By inspection of Fig. 7, the angular energy distributions are remarkably well fitted by the function of Eq. (2) in the interval  $0 < \theta \lesssim 3.4^\circ$ , i.e., in the angular region occupied by the beam of the jet. At smaller latitudes ( $5^\circ \lesssim \theta \lesssim 8^\circ$ ) the model data separates from the fitting function and presents systematically larger values than the latter. Indeed, the data in such an interval can be well fitted by a simple power law, with a slope in the range  $[-2.1, -2.5]$  (see the inset in Fig. 7). The deviation from the SBP function in this angular range is due to the contribution of the expanding, mildly relativistic cocoon. This cocoon contribution shows up more clearly (the energy distribution tends to flatten in the range  $\theta > 5^\circ$ ) if we lower the thresholds on the values of  $h\Gamma$  and  $v_r$  used to compute the angular energy distribution of each model. However, as we argued before, lowering these thresholds too much will catch up contributions from numerical cells whose asymptotic Lorentz factor is too small to account for typical afterglow.

Low metallicity models 16TB, 16TC, and 16OC, are

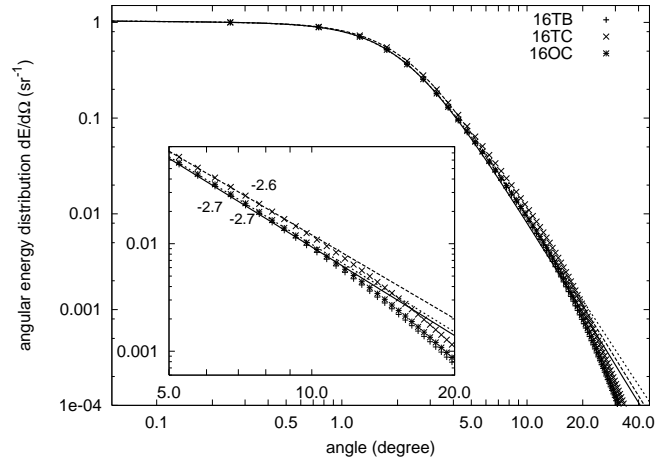


FIG. 8.— Same as Fig. 7, but for the models, 16TB, 16TC, and 16OC.

also well fit by the function of Eq. (2) in roughly the same interval as the solar metallicity models (Fig. 8). The values of the fit parameters are comparable to those of type-H models, with which they share a very similar progenitor mass ( $\sim 15M_\odot$ ). However, in these models, the cocoon contribution, which can be fit by a simple power-law with a slope  $\sim -2.6$  between  $5^\circ \lesssim \theta \lesssim 8^\circ$  (Fig. 8 inset) shows a faster decay of  $dE/d\Omega$  than type-H models for  $\theta > 8^\circ$ . The reason for this difference is the much deeper density drop of low-metallicity models close to the star surface (Fig. 2) compared with type-H models (Fig. 1). The density of low-metallicity models in the region  $3 \times 10^{10} \text{ cm} \lesssim r \lesssim 4 \times 10^{10} \text{ cm}$  is  $\sim 100$  times smaller than in type-H models. Hence, the beam of jets in such low-metallicity progenitors becomes much more ballistic than the corresponding beams of jets in the type-H group. Since more ballistic beams reduce the sideways expansion of their cocoons, this explains that the angular energy distribution in low-metallicity stars is more narrowly concentrated than in solar-metallicity, type-H progenitors.

In order to show more clearly the existence of correlations between the properties of the progenitor star and the  $dE/d\Omega$  distribution, we show in Fig. 9 the dependence of the postbreak slope  $\alpha_h$  and on the stellar progenitor mass  $M$ . There exists a correlation between  $\alpha_h$  and  $M$ , such that the slope of lighter progenitors is steeper than that of heavier ones. There is roughly a linear dependence of  $\alpha_h$  on  $M$ , which displays a relatively large dispersion. The reason for the dispersion being that for very similar values of the total progenitor mass, the rest-mass density radial profiles can be appreciably different (see, e.g., Figs. 1 and 2). This is particularly true in heavy progenitor models (including type-H and low metallicity models). For the prebreak slope  $\alpha_l$  we find no obvious correlation with the progenitor mass, but in all the models considered here is very small ( $\alpha_l \simeq 0$ ; Tab. 1).

We have also investigated the dependence of the slope  $\alpha_h$  and  $\alpha_l$  on the mass loss rate  $\dot{M}$  assumed in models of Woosley & Heger (2006) (see Tab. 1). Figure 10 shows that there exist a good correlation between  $\alpha_h$  and  $\dot{M}$ ,

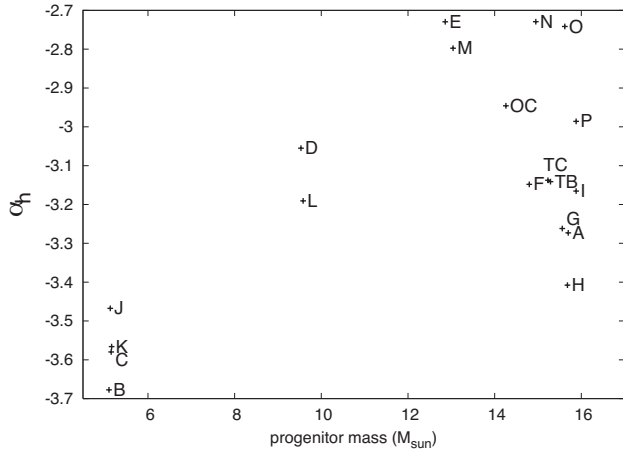


FIG. 9.— Dependence of the index  $\alpha_h$  on the total mass of the progenitor. We identify the models by the last letter in the model name, e.g., the label 'A' stands for model HE16A. The labels 'TB', 'TC', and 'OC' stand for the models 16TB, 16TC, and 16OC, respectively.

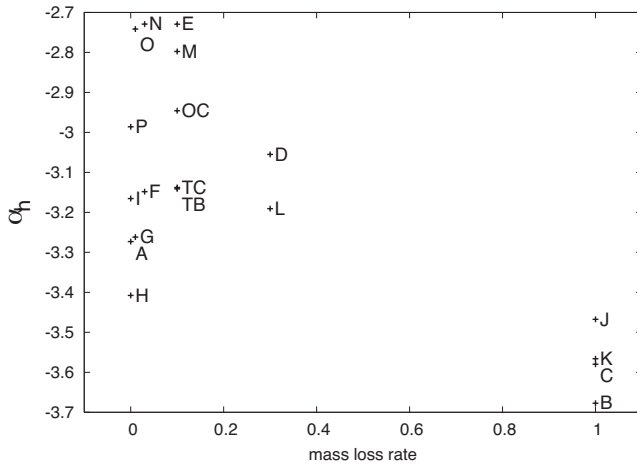


FIG. 10.— Dependence of the index  $\alpha_h$  on the mass loss rate in units of the *typical* mass loss rate considered by Woosley & Heger (2006). The naming convention is the same as in Fig. 9.

while  $\alpha_l$  seems to be independent of  $\dot{M}$ . The  $\alpha_h - \dot{M}$  correlation tells us that, models with a larger mass loss rate possess a steeper slope. This is not surprising considering the previously found correlation between  $\alpha_h$  and  $M$ , since the stellar progenitor mass is mostly determined by the amount of mass lost in the form of winds during the latest stages of its evolution.

We have not found any other good correlation between the fit parameters (other than  $\alpha_h$ ) and the gross properties of the progenitors (radius, average density, total angular momentum, rotation period, mass of the iron core, etc.).

We shall note that the angular distribution  $dE/d\Omega$  is not directly observable. Instead, the isotropic equivalent angular energy per solid angle  $dE/d\Omega|_{\text{iso}}$  can be detected. Figure 11 shows the equivalent isotropic angular energy distribution for prototype models belonging to the types L, M and H, normalized to the value of the distribution at  $\theta = 0.25^\circ$ . As can be seen from Fig. 11 (see also Tab. 1), the values of  $\alpha_{l,\text{iso}}$  are also negative for the

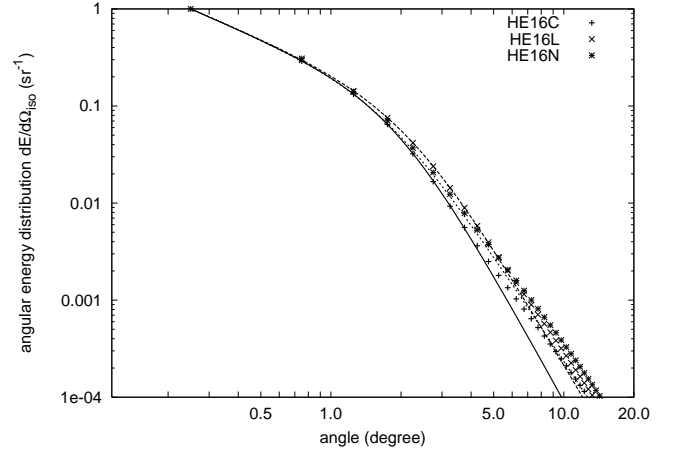


FIG. 11.— Equivalent isotropic angular energy distribution of the jets when the head of the jet reaches the outer computational boundary. The models shown are HE16C, HE16L, and HE16N, along with their corresponding fitting functions (with lines).

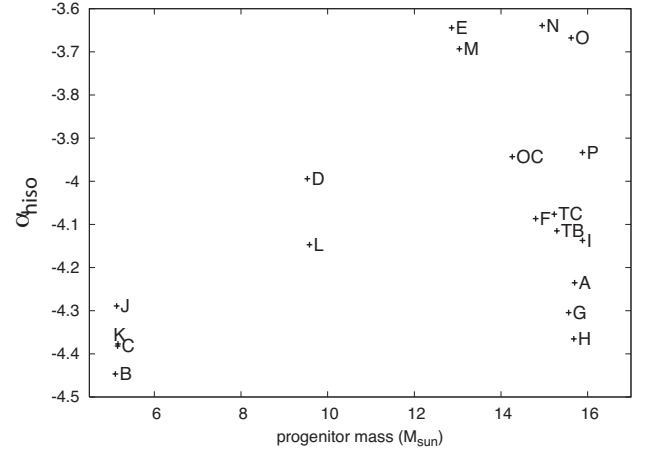


FIG. 12.— Same as Fig.9 but for the equivalent isotropic energy distribution.

$dE/d\Omega|_{\text{iso}}$ , while the corresponding values  $\alpha_l$  are close to zero for  $dE/d\Omega$  (approximately,  $\alpha_{l,\text{iso}} \simeq \alpha_l - 1$ ). This happens because of the small value of the solid angles close to the symmetry axis, which makes systematically larger the higher latitude values of  $dE/d\Omega|_{\text{iso}}$  than those of  $dE/d\Omega$ . The values of  $\alpha_{h,\text{iso}}$  are systematically smaller than the respective  $\alpha_h$  values (roughly,  $\alpha_{h,\text{iso}} \simeq \alpha_h - 1$  in our standard resolution runs). Given the tight relations of the slopes in the  $dE/d\Omega$  and  $dE/d\Omega|_{\text{iso}}$  distributions, it is not surprising to find that there exists a good correlation between  $\alpha_{h,\text{iso}}$  and  $M$  (Fig. 12) which follows the same qualitative trend as the correlation between  $\alpha_h$  and  $M$ .

To sum up our findings so far, we realize that the values of the parameters of the fit function (Eq.2) are chiefly correlated with the mass of the progenitor. In type-L progenitors, the velocity of propagation of the jet is larger than in more massive models, which results in jets developing more massive and hotter cocoons in type-M

and type-H models than in light progenitors<sup>4</sup>. This fact is evident by looking at Fig. 13, where the pressure in the cocoon of the model HE16N is higher than that in the model HE16C in the course of the propagation of the jet up to the progenitor surface. The differences in the propagation velocity of the injected jets are set, to a large extent, by the differences in the average density between progenitors of different mass. The less massive progenitors of our sample (type-L models) tend to have the smaller average densities (see, e.g., Fig. 1, where model HE16C displays a smaller density than model HE16N at every radial point). Consistently, jets propagating in type-L progenitors are faster as can be observed in Fig. 14. However, the time needed to reach the progenitor surface presents a dependence with the progenitor mass with a much larger scatter (Fig. 15). Particularly, models HE16A, HE16F, HE16G and HE16H, all of which belong to the type-H group, display a progenitor crossing time comparable to that of the jets in the type-L group (although its average propagation velocity is comparable to that of models of type-H). That's the reason why these models appear as *outliers* in the correlations between the slope  $\alpha_h$  and the progenitor mass (Figs. 9 and with the mass-loss rate (Fig. 10). Since more massive progenitor stars yield hotter cocoons, once the cocoon is erupted through the stellar surface, it undergoes a larger lateral expansion (compare models HE16C and HE16N in the lower panels of Fig. 1), i.e., the energy carried by the jet spreads towards lower latitudes. This explains why the energy per solid angle is more concentrated towards the axis when the jet crosses a low mass progenitor.

If we assume that the detectability of an event, for an observer looking such event at a certain viewing angle ( $\theta$ ), is proportional to  $dE/d\Omega|_{\text{iso}}(\theta)$  (see, e.g., Janka et al. 2006), it turns out that  $\theta$  should be rather small ( $\lesssim 2^\circ$ ; Fig. 16) to observe and event produced in collapsar progenitors (note that the flanks of  $dE/d\Omega|_{\text{iso}}$  distribution are quite steep and, thus, it is very unlikely to detect events which are not directly pointing towards the observer). Jets produced in type-L progenitors exhibit narrower observability profiles than those injected in more massive stars (c.f., compare the profiles of models HE16C and HE16N in Fig. 16). Therefore, it is more unlikely to detect off-axis events produced in light progenitors than in more massive ones. Alternatively, we may state the the lower degree of collimation of relativistic jets in high-mass stars results in a higher probability of observing an event from a high-mass progenitor than a low-mass progenitor. We also find that the metallicity has little influence on the observability, because for similar progenitor masses, solar-metallicity models and low metallicity ones display almost identical observability angular profiles (Fig. 16).

We also notice the very different observability profiles of jets produced in collapsars and jets produced in rem-

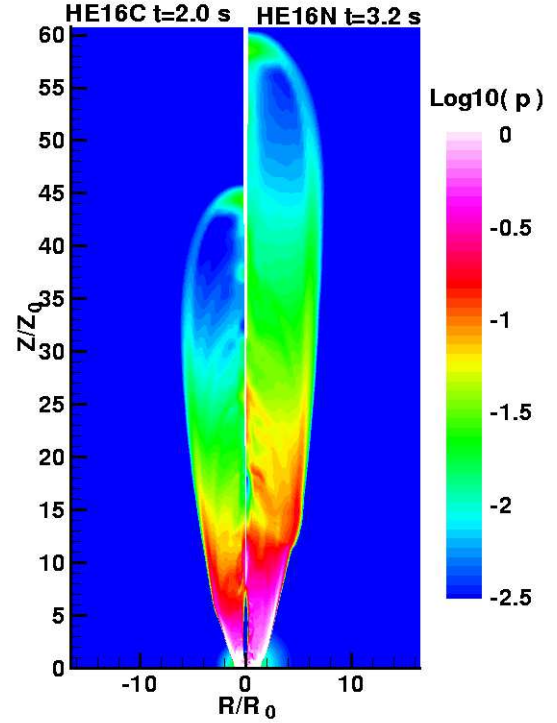


FIG. 13.— Pressure contours of models HE16C (left: at  $t = 2.0$  s) and HE16N (right: at  $t = 3.2$  s), when the head of the jet reaches progenitor surface in each model, i.e., at shock break out. Both, the vertical and the horizontal axis are scaled by  $R_0 = Z_0 = 10^9$  cm. The radii of the progenitors are  $4.73 \times 10^{10}$  cm and  $6.13 \times 10^{10}$  cm for the models HE16C and HE16N, respectively. At the same distance  $Z/Z_0$  from the injection nozzle, the pressure in both the jet and in the cocoon is higher for model HE16N than for model HE16C. This fact explains the larger lateral expansion after shock break out in model HE16N than in model HE16C.

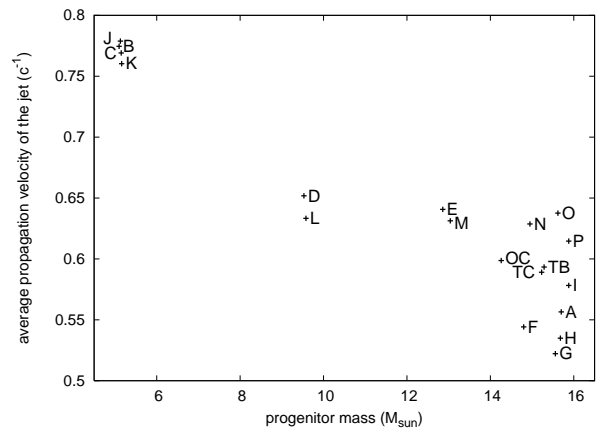


FIG. 14.— Dependence on the progenitor mass of the average propagation velocity of the jet in the star. The average propagation velocity is defined as the ratio between the progenitor radius  $r_*$  and the time it takes the head of the jet to propagate up to  $r_*$ . The labeling convention is the same as in Fig. 9.

<sup>4</sup> Since the injected mass flux is the same in all models, jets which take longer to reach the stellar surface (i.e., jets with small propagation speed) are more massive and, hence their cocoons are also heavier. On the other hand, the slower jets develop stronger reverse shocks than the faster ones, because the injected fluxes of mass, momentum and energy are the same in all our models. Thus, the jet matter is compressed more in the former than in the latter case, which explains why the matter in the cocoon is hotter in jets with smaller propagation speeds.

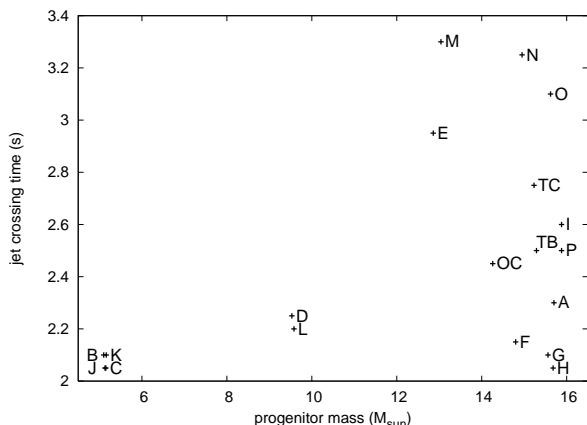


FIG. 15.— Dependence on the progenitor mass of the time employed by the jet to reach the progenitor surface. The labeling convention is the same as in Fig. 9.

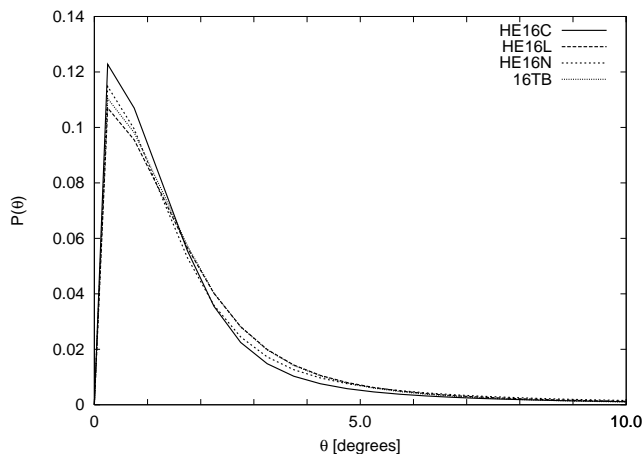


FIG. 16.— Detectability of the models HE16C, HE16L, HE16N and 16TB.

nants of mergers of compact objects. In the latter case, a non-negligible observability is obtained in the viewing angle interval  $2^\circ \lesssim \theta \lesssim 13^\circ$ , because of the larger half-opening angles of the outflows originated in progenitors of short GRBs (see Fig. 2 of Janka et al. 2006). Another relevant difference is that collapsar-jets show a detectability with a fast rise close to  $\theta = 0$ , followed by a shallower decay beyond the most probable detection angle  $\sim 0.5^\circ$ . In contrast, most jets produced in merger remnants tend to decay very abruptly beyond the most likely observing angle, and have an observability rise much more moderate than that of collapsar-jets. The reason for this difference is the much shallower decay of the isotropic equivalent energy at the flanks of the beam in collapsar-jets than in jets from merger remnants.

#### 4. CONCLUSIONS AND DISCUSSION

In this paper we explore the relation of the dynamical properties of ultrarelativistic jets generated in collapsars with the properties of the progenitor stars in which such jets propagate. We have particularly focused on the correlations that exist between the angular profile of the energy per solid angle (as seen in the afterglow phase)

and the properties of the progenitors. Along the way, we have pointed out which is the relevance of the fact that our numerical models are set up with a finite injection half-opening angle.

Using a non-zero injection angle affects the way in which the conversion of internal-to-kinetic energy takes place. If the flow is injected parallel to the polar axis, the development of reconfinement shocks happens closer to the injection nozzle than if the flow is injected radially within a cone of finite half-opening angle. When the recollimation shock occurs far away from the nozzle, the unshocked beam flow accelerates along a larger distance in a rarefaction that precedes such shock. Thus, the beam reaches there larger Lorentz factors than if the jet is injected parallel to the polar axis. The dissipation in cross shocks acts by simply recycling part of the kinetic energy of the outflow into thermal energy. The thermal energy is not lost, since the jet propagation is roughly adiabatic inside of the progenitor (radiation losses are negligible there). Instead, this thermal energy can be further converted into kinetic energy at larger distances. This process may happen several times before the outflow becomes transparent and radiation can freely escape. This explains why, in spite of the differences in the beam dynamics, all models (independent of the injection half-opening angle; c.f., Mizuta et al. 2006) develop a roughly similar propagation speed and, by the time they reach the head of the jet, the gross properties of the outflow are similar.

We have estimated the angular distribution of energy per solid angle in the afterglow phase by extrapolation of the state of our models when they reach a distance of  $\sim 10^{11}$  cm. This extrapolation relies on the fact that the jets develop a rough self-similar behavior soon after they emerge from the progenitor surface. Our results show that the equivalent isotropic energy per solid angle  $dE/d\Omega|_{\text{iso}}$  is only partly consistent with that of Lazzati & Begelman (2005). However, the results in this paper do appear to be consistent with previous numerical simulations such as those of Zhang et al. (2004) and Morsony et al. (2007). Lazzati & Begelman (2005) obtain that the angular energy distribution displays a relatively flat core which is flanked by a region where  $dE/d\Omega|_{\text{iso}} \propto \theta^{-2}$ . Our results show that the core of the distribution (close to  $\theta = 0^\circ$ ) is not flat (but decays as  $\theta^{-1}$ ) and that the energy per solid angle decays much faster than  $\theta^{-2}$  (it does it as  $\theta^\kappa$ , with a value of  $\kappa \lesssim -3.6$  depending on the mass of the progenitor; see below). We can fit the  $dE/d\Omega|_{\text{iso}}$ -data with SBP functions up to  $\theta \lesssim 3.4^\circ$ . At smaller latitudes, a simple power-law with a slope close to  $-2.6$  fits better the data. In this region ( $4.5^\circ < \theta < 8^\circ$ ), the cocoon contribution is the dominant (at smaller values of  $\theta$ , the beam of the jet dominates the energetics), and we find there the best consistency with the model of Lazzati & Begelman (2005).

We have correlated the properties of the angular  $dE/d\Omega|_{\text{iso}}$  distribution of the jet with the fundamental parameters of the progenitor star in which the jet has propagated. We find that the shape of the distribution is mostly influenced by the mass of the progenitor. When the mass of the progenitor is small ( $M \sim 5M_\odot$ ), because of the occurrence of large mass losses due to winds in the latest stages of the star's evolution, then  $dE/d\Omega|_{\text{iso}}$

decays faster with  $\theta$  than if the mass of the progenitor is large ( $M \sim 15M_{\odot}$ ). We find that the reason for this behavior is that the average density of the progenitors tends to grow (approximately) with the mass. This means that the average jet propagation speed inside of the star is smaller, the larger is the mass. A smaller jet propagation speed results into thicker and hotter cocoons, since we fix the same mass, momentum and energy fluxes at the nozzle for all models. Also the beam of the jet in the more massive progenitors is wider. This is the reason why low mass progenitors develop narrower  $dE/d\Omega|_{\text{iso}}$  profiles than high mass ones. The difference in the collimation of the energy distributions resulting from low and high mass progenitors has a direct influence on the number of observed events. We expect to see more events produced in heavy progenitors than in low mass ones.

One could question whether the correlation that we have found between the mass of the progenitor and the width of the  $dE/d\Omega|_{\text{iso}}$  is an artifact of our numerical set up. We are fixing the luminosity of the jet to be the same independent of the progenitor mass. However, progenitors of different mass may develop central engines which release different power. A good proxy of the power of the central engine is the mass of the iron core of the progenitor. One may expect that the collapse of more massive iron cores results into larger central compact objects. If the power released by the central engine is dominated by the size of the central compact object, then models with more massive iron cores could release a larger power than models with low mass cores. Then, how do we justify our numerical assumption that the power injected in the jet is roughly independent of the progenitor's mass?. In support of our point we argue that, first, according to Woosley & Heger (2006) data, there is not a one to one correlation between the mass of the iron core and the mass of the progenitor and, second, the iron mass varies by less than a 30% in all the models considered here, while the total mass can be different by a factor of 3. Thus, within the simplifications we do in our models, the assumption of a common luminosity independent of the mass of the progenitor is justified.

Irrespective of these two arguments, if heavier progenitors would result into more luminous central engines, we shall point out that this trend will also result into wider jets and cocoons. This is a result early pointed out by Aloy et al. (2000), were it was shown that, taking the same progenitor, but increasing the luminosity of the central engine by a factor of 10, results into thicker cocoons than in cases in which the luminosity is more moderate. The reason being that the release of a large power triggers large amplitude Kelvin-Helmholtz instabilities at the basis of the outflow, which transfer a large fraction of the momentum of the beam to a thicker shear

layer between the beam and the cocoon. Effectively, this process widens the cross sectional area of the beam, reducing its propagation speed and, consistently inflating larger cocoons.

We have also found, that comparing progenitors of similar mass, the metallicity of the star has a small impact on the extrapolated  $dE/d\Omega|_{\text{iso}}$  profiles. The collimation of the jet is similar regardless of the stellar metallicity. However, the cocoon is more narrowly collimated in low-metallicity stars, because of the large density drop close to their surfaces. This reduced density makes the jets in low-metallicity stars much more ballistic, once they break out the stellar surface, than in solar-metallicity progenitors. Unfortunately, this difference might not be observable, since it happens in regions where the energy per solid angle is much smaller than at the jet core (unless orphan afterglows could be detected; see, e.g., Totani & Panaitescu 2002; Rossi, Perna & Daigne 2008).

Finally, we have found significant differences between the  $dE/d\Omega|_{\text{iso}}$  profiles of collapsar-jets and those of jets produced in merger remnants (i.e., between the angular energy distribution of jets associated to long and to short GRBs). Collapsar-jets are more narrowly collimated than jets of merger remnants, and the decay of  $dE/d\Omega|_{\text{iso}}$  beyond the central flat core is much steeper in the latter than in the former. This intrinsic difference manifest itself as a larger chance of detectability of jets from merger remnants at viewing angles up to  $\theta \sim 12^\circ$ , while, on the other hand, collapsar-jets could hardly be seen off-axis.

We would like to thank A. Heger for his kindness to allow us to use his progenitor models for this study. We would like to thank Dr. Hanawa for his helpful comments. We also thank the referee for his/her useful comments that helped to improve this paper. This work is partly supported by the Grants-in-Aid of the Japanese Ministry of Education, Science, Culture, and Sport (19540236, 20041002, 20340040 A.M.), the grants of the Spanish Ministry of Science and Innovation CSD2007-00050 and AYA2007-67626-C03-01. M. A. A. is a Ramón y Cajal fellow of the Spanish Ministry of Education and Science. The calculations were carried out on a NEC SX8, at the Cybermedia Center, Osaka University, on a NEC SX8, at Yukawa Institute for theoretical physics, Kyoto University, on the Space Science Simulator (NEC SX6), at the Japan Aerospace Exploration Agency, and on a NEX SX9, at the Center for Computational Astrophysics, National Astronomical Observatory of Japan.

## APPENDIX

### ON THE CHOICE OF NUMERICAL RESOLUTION

The main purpose of this Appendix is to justify the choice of numerical resolution that we have used in the main body of this paper. We have picked up three models, HE16C, HE16L and HE16N (representative of the models of the respective types-L, -M and H) and performed a resolution study by progressively increasing the numerical resolution. Our standard models have a working resolution  $N_r \times N_\theta = 1000 \times 180$  zones. The standard computational grid is uniform in both  $\log r$ - and  $\theta$ -coordinates. In addition to the standard resolution, two higher resolutions have been considered.

First, we compute models HE16C-M, HE16L-M, and HE16N-M (Tab. 1), which have an intermediate resolution of

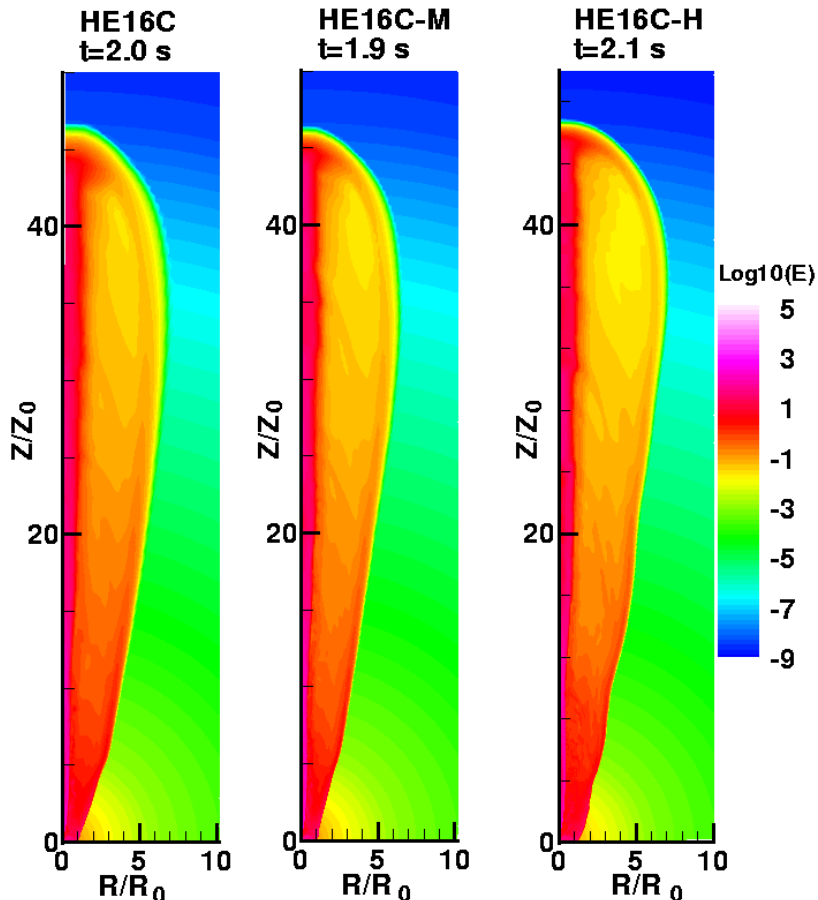


FIG. 17.— Contours of the energy density for the same model run at three different resolutions, corresponding to models HE16C, HE16C-M, and HE16C-H. The jet in all cases is about to break the surface of the star ( $R_* = 4.75 \times 10^{10}$  cm). Since the jet propagates at slightly different speed depending on the resolution, the three snapshots correspond to slightly different evolutionary times. Both, the vertical and the horizontal axis are scaled by  $R_0 = Z_0 = 10^9$  cm.

$N_r \times N_\theta = 1500 \times 180$  zones. In these models the radial grid is uniform in  $\log r$  and the smallest radial grid spacing is  $\Delta r = 7.5 \times 10^5$  cm, i.e.,  $3/4$  times smaller than that of our standard resolution cases. The polar grid possesses a uniform region close to the symmetry axis ( $0^\circ < \theta < 40^\circ$ ), where  $\Delta\theta = 1/3^\circ$ , followed by a uniformly spaced region in  $\log\theta$  ( $30^\circ < \theta < 90^\circ$ ). The reason to consider two different regions in the  $\theta$ -spacing is that all our jet models develop cocoons whose angular extension is  $\theta < 30^\circ$ , i.e., all the dynamics develops in a wedge covered by a finer mesh in our computational grid. Thus, an increased resolution in the abovementioned wedge surrounding the polar axis yields an effective increase of the numerical resolution in the whole computational grid.

Even higher resolution models (HE16C-H, HE16L-H, and HE16N-H) have also been computed. In this case, the grid consists of  $N_r = 2000$  zones uniformly spaced in  $\log r$ , with a minimum radial grid spacing  $\Delta r = 5 \times 10^5$  cm, i.e., one half of the width of smallest radial spacing of the standard resolution case. We take in this case  $N_\theta = 180$  zones, also split in two regions: a uniform grid in the interval  $0^\circ < \theta < 30^\circ$  ( $\Delta\theta = 0.25^\circ$ ), followed by a uniformly spaced region in  $\log\theta$  ( $30^\circ < \theta < 90^\circ$ ).

Going to even larger resolutions in the  $\theta$ -direction increases the total computational time up to prohibitive limits due to the increased number of time steps associated to the fulfillment of the Courant condition.

We note that the jet dynamics is rather independent of the resolution, and also the gross morphological features are converged at the standard resolution, though, of course, finer details show up both in the cocoon and in the beam (see Fig. 17). Therefore, when we take radial averages to compute the angular energy distribution of our models (Eq. 1), the differences are relatively small (see below), and our standard resolution models can be considered to be sufficiently resolved to account for such global energetic properties. The time-scales to cross the progenitor and/or to reach the outer computational boundary (at  $r = 10^{11}$  cm) are slightly different from each other.

Figure 18 shows the isotropic equivalent angular energy distributions of models computed with three different resolutions. In all cases, a SBP function (Eq. 2) fits properly the data up to  $\theta < 3.4^\circ$ . At larger latitude, the contribution of the expanding cocoon component dominates. Since each distribution is normalized independently to its absolute maximum, the distributions corresponding to different resolutions do not overlap, but they show the same shape. The fitting parameters for the higher resolution cases are also listed in Tab. 1. There, we can see that the same

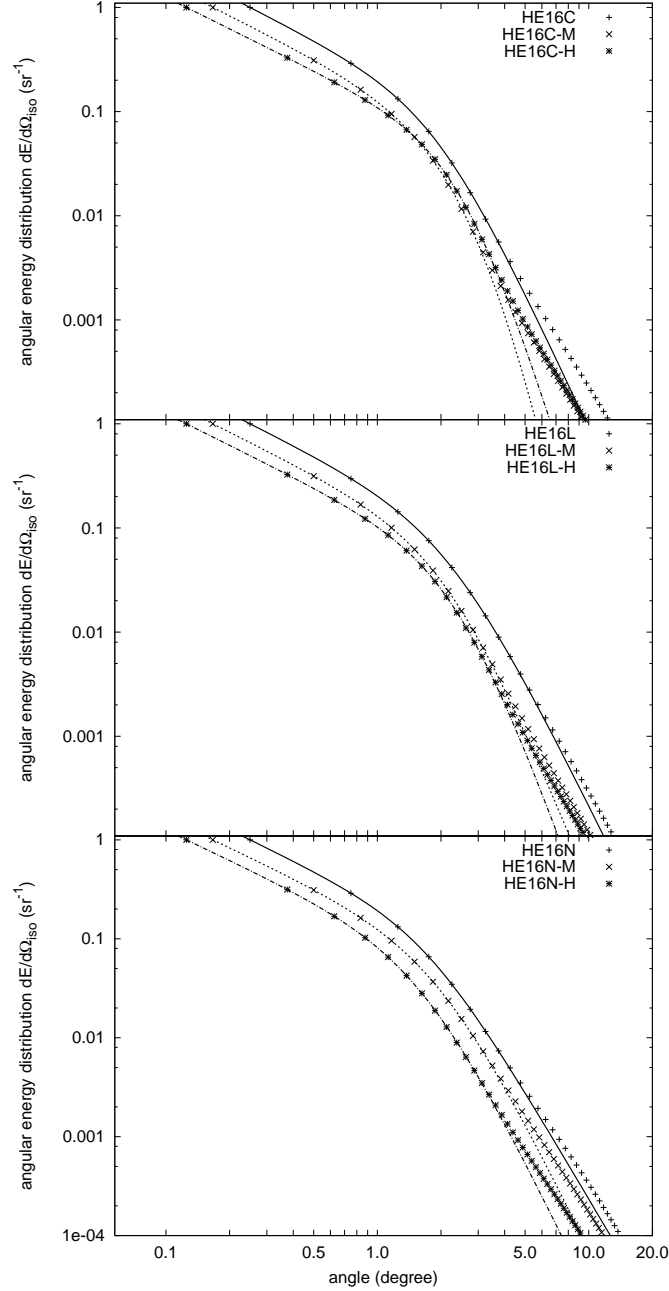


FIG. 18.— Comparison of the angular energy distributions of prototype models (HE16C (top), HE16L (middle), and HE16L (bottom)) run with different computational resolutions. The solid, dashed, and dotted lines show the fitting functions of Eq. 2 corresponding to models computed with the standard, the middle, and the highest resolution, respectively.

correlations found in models with the standard resolution are reproduced at higher resolutions, namely, the correlation between  $\alpha_h$  or  $\alpha_{h,iso}$  with the progenitor mass (Sect. 3.2). However, at higher resolution, we could guess additional correlations which are not obvious in models run with the standard resolution. Particularly, the parameters  $\theta_0$  and  $\theta_{0,iso}$  become smaller as the progenitor mass increases. This trend is however, an artifact of the models chosen as prototypes of each mass type. They are such, that the radius of the progenitor roughly grows with the mass. As pointed out by Aloy et al. (2000), progenitors with larger radii provide a larger inertial confinement which prevents the lateral expansion of the jet. Hence, for the models chosen in this resolution study, a larger progenitor mass yields better collimated jets. Taking the whole sample of models, but run at higher resolution, the correlations between  $\theta_0$  or  $\theta_{0,iso}$  would not exist.

## REFERENCES

- Aloy, M. A., Müller, E., Ibáñez, J. M., Martí, J. M., & MacFadyen, A. 2000, *ApJ*, 531, L119
- Aloy, M.-A., Ibáñez, J.-M., Miralles, J.-A., & Urpin, V. 2002, *A&A*, 396, 693
- Aloy, M. A., & Martí, J. M. 2002, in *Relativistic Flows in Astrophysics*, eds. A. W. Guthmann, M. Georganopoulos, A. Marcowith & K. Manolakou. *Lecture Notes in Physics*, 589, 197
- Aloy, M. A., & Obergaulinger, M. 2007, *Rev. Mex. Astron. y Astrof.*, 30, 96
- Aloy, M. A., & Rezzolla, L. 2006, *ApJ*, 640, L115
- Berger, E., Kulkarni, S. R., & Frail, D.A. 2001, *ApJ*, 560, 652
- Campana, S., et al. 2006, *Nature*, 442, 1008
- Della Valle, M., et al., 2006, *Nature*, 444, 1050
- Frail, D. A., et al., 2002, *ApJ*, 565, 829
- Fruchter, A. S., et al., 2006, *Nature*, 441, 463
- Fynbo, J. P. U., et al., 2006, *Nature*, 444, 1047
- Gal-Yam, A., et al., 2006, *Nature*, 444, 1053
- Ghisellini, G., Celotti, A., Ghirlanda, G., Firmani, C., & Nava, L. 2007, *MNRAS*, 382, L72
- Iwamoto, K., et al. 1998, *Nature*, 395, 672
- Janka, H.-T., Aloy, M.-A., Mazzali, P. A., & Pian, E. 2006, *ApJ*, 645, 1305
- Kobayashi, S., Piran, T., & Sari, R. 1999, *ApJ*, 513, 669
- Komissarov, S. S., & Falle, S. A. E. G. 1997, *MNRAS*, 288, 833
- Komissarov, S. S., & Falle, S. A. E. G. 1998, *MNRAS*, 297, 1087
- Komissarov, S. S., & Barkov, M. V. 2007, *MNRAS*, 382, 1029
- Galama, T. J., et al. 1998, *Nature*, 395, 670
- Lazzati, D., & Begelman, M. C. 2005, *ApJ*, 629, 903
- Le Floc'h, E. 2004, *ApJS*, 154, 170
- MacFadyen, A. I., & Woosley, S. E. 1999, *ApJ*, 524, 262
- McKinney, J. C. 2006, *MNRAS*, 368, 1561
- Martí, J. M. A., Mueller, E., Font, J. A., Ibanez, J. M. A., & Marquina, A. 1997, *ApJ*, 479, 151
- Mazzali, P. A., et al. 2006, *Nature*, 442, 1018
- Mimica, P., Aloy, M. A., Agudo, I., Martí, J. M., Gómez, J. L., Miralles, J. A., 2008, arXiv:0811.1143
- Mizuno, Y., et al., 2004, *ApJ*, 606, 395
- Mizuta, A., Yamada, S., & Takabe, H., 2004, *ApJ*, 606, 804
- Mizuta, A., Yamasaki, T., Nagataki, S., & Mineshige, S. 2006, *ApJ*, 651, 960
- Morsony, B. J., Lazzati, D., & Begelman, M. C. 2007, *ApJ*, 665, 569
- Nagataki, S., Takahashi, R., Mizuta, A., & Takiwaki, T. 2007, *ApJ*, 659, 512
- Piran, T. 1999, *Phys. Rep.*, 314, 575
- Proga, D., et al., 2003, *ApJ*, 599, L5
- Ramirez-Ruiz, E., MacFadyen, A. I., & Lazzati, D. 2002a, *MNRAS*, 331, 197
- Ramirez-Ruiz, E., Celloti, A., & Rees, M. J. 2002b, *MNRAS*, 337, 1349
- Rees, M. J., & Meszaros, P. 1992, *MNRAS*, 258, 41
- Rossi, E.M., E.M., Perna, R., Daigne, F. 2008, *MNRAS*, 390, 675
- Stanek, K. Z., et al. 2003, *ApJ*, 591, L17
- Takiwaki, T., Kotake, K., & Sato, K. 2009, *ApJ*, 691, 1360
- Tominaga, N. et al., 2007, *ApJ*, 657, L77
- Totani, T., Panaitescu, A. 2002, *ApJ*, 576, 120
- Woosley, S. E. 1993, *ApJ*, 405, 273
- Woosley, S. E. 2000, in *AIP Conf. Proc. 526, Gamma-ray Bursts*, ed. R. M. Kippen, R.S. Mallozzi, & G. J. Fishman (Melville: AIP), 555
- Woosley, S. E., & Heger, A., 2006, *ApJ*, 637, 914
- Yoon, S.-C., & Langer, N. 2005, *A&A*, 443, 643
- Yoon, S.-C., Langer, N. & Norman, C. 2006, *A&A*, 460, 199
- Zhang, W., Woosley, S. E., & MacFadyen, A. I. 2003, *ApJ*, 586, 356
- Zhang, W., Woosley, S. E., & Heger, A. 2004, *ApJ*, 608, 365

TABLE 1

PROPERTIES OF THE PRE-SUPERNOVA MODELS TAKEN FROM WOOSLEY & HEGER (2006) FOR OUR STUDY. COLUMNS 1-4, LIST THE MODEL NAME, THE MASS LOSS RATE (IN THE SAME UNITS AS WOOSLEY & HEGER 2006), THE TOTAL MASS, AND THE RADIUS AT PRE-SUPERNOVA STAGE. COLUMNS 5-9, DISPLAY THE BEST PARAMETERS OF THE SBP (EQ. 2) USED TO FIT THE ANGULAR ENERGY DISTRIBUTION PER SOLID ANGLE (EQ. 1). FINALLY, COLUMNS 10-14, SHOW THE BEST FIT PARAMETERS FOR THE ANGULAR DISTRIBUTION OF EQUIVALENT ISOTROPIC ENERGY PER SOLID ANGLE. THE LAST SIX ROWS CORRESPOND TO SOME PROTOTYPE MODELS WHICH HAVE BEEN RUN WITH HIGHER NUMERICAL RESOLUTION. MODELS WHOSE NAME ENDS WITH "-M" AND "-H" HAVE BEEN RUN WITH NUMERICAL RESOLUTIONS OF  $1500 \times 180$  AND  $2000 \times 180$  GRID POINTS, RESPECTIVELY (SEE APPENDIX).

model	mass loss	total mass / $M_{\odot}$	Radius / $10^{10}$ cm	$\alpha_l$ / $10^{-2}$	$\alpha_h$	$A/10^{53}$ ergs	$\theta_0$	$n$	$\alpha_{l_{iso}}$	$\alpha_{h_{iso}}$	$A_{iso}/10^{57}$ ergs	$\theta_{0_{iso}}$	$n_{iso}$
HE16A	0	15.70	3.86	-1.22	-3.27	8.65	2.37	-0.686	-1.01	-4.24	2.45	2.35	-0.696
HE16B	1.0	5.10	4.91	-1.72	-3.68	6.02	2.12	-0.632	-1.02	-4.45	2.14	2.02	-0.694
HE16C	1.0	5.15	4.75	-2.99	-3.58	6.61	2.03	-0.706	-1.03	-4.38	2.40	1.95	-0.765
HE16D	0.3	9.53	4.42	-1.22	-3.05	8.84	2.21	-0.746	-1.01	-3.99	2.72	2.18	-0.768
HE16E	0.1	12.86	5.71	-2.60	-2.73	9.64	1.84	-0.896	-1.03	-3.64	3.64	1.80	-0.942
HE16F	0.03	14.80	3.52	-1.33	-3.15	9.28	2.41	-0.726	-1.01	-4.09	2.63	2.37	-0.746
HE16G	0.01	15.56	3.31	-1.27	-3.26	8.55	2.44	-0.719	-1.01	-4.30	2.24	2.47	-0.705
HE16H	0	15.68	3.31	-1.71	-3.41	8.96	2.34	-0.690	-1.02	-4.37	2.58	2.32	-0.701
HE16I	0	15.88	4.54	-1.21	-3.17	8.12	2.33	-0.714	-1.01	-4.14	2.32	2.32	-0.722
HE16J	1.0	5.13	4.81	-3.64	-3.47	7.23	1.89	-0.764	-1.04	-4.29	2.77	1.82	-0.824
HE16K	1.0	5.16	4.81	-3.49	-3.57	6.67	2.02	-0.741	-1.04	-4.38	2.39	1.95	-0.798
HE16L	0.3	9.58	4.18	-1.01	-3.19	8.51	2.27	-0.707	-1.01	-4.15	2.53	2.24	-0.721
HE16M	0.1	13.04	6.29	-2.29	-2.80	8.89	1.93	-0.851	-1.03	-3.69	3.24	1.88	-0.903
HE16N	0.03	14.95	6.17	-2.91	-2.73	9.92	1.79	-0.914	-1.03	-3.64	3.86	1.75	-0.965
HE16O	0.01	15.62	5.96	-1.88	-2.74	9.11	1.99	-0.855	-1.02	-3.67	3.16	1.94	-0.891
HE16P	0	15.88	4.63	-1.40	-2.99	9.78	2.18	-0.762	-1.01	-3.93	3.05	2.15	-0.781
16TB	0.1	15.29	4.45	-1.42	-3.14	8.38	2.19	-0.733	-1.01	-4.11	2.55	2.18	-0.741
16TC	0.1	15.23	4.87	-1.46	-3.14	7.51	2.30	-0.735	-1.02	-4.08	2.22	2.27	-0.754
16OC	0.1	14.26	4.42	-1.62	-2.95	9.05	2.09	-0.798	-1.02	-3.94	2.85	2.09	-0.798
HE16C-M	1.0	5.15	4.75	-0.72	-5.77	6.71	2.70	-0.486	-1.01	-9.81	0.310	3.43	-0.241
HE16L-M	0.3	9.58	4.18	-1.16	-4.45	11.8	2.40	-0.572	-1.01	-5.04	2.97	2.29	-0.569
HE16N-M	0.03	14.95	6.17	-1.27	-3.33	17.9	1.65	-0.685	-1.01	-4.41	3.64	2.06	-0.645
HE16C-H	1.0	5.15	4.75	-1.99	-6.18	4.40	2.64	-0.377	-1.00	-7.76	1.08	2.98	-0.397
HE16L-H	0.3	9.58	4.18	-1.04	-3.90	11.0	2.22	-0.600	-1.01	-6.36	2.04	2.74	-0.446
HE16N-H	0.03	14.95	6.17	-1.18	-3.22	12.4	1.96	-0.704	-1.01	-4.62	5.74	1.79	-0.596